Research Square

Preprints are preliminary reports that have not undergone peer review.
They should not be considered conclusive, used to inform clinical practice,
or referenced by the media as validated information.

An Innovative Thermal Decomposition Method for the Deter-mination of Exchangeable NH_4^+ in Zeolites and SAR Estimation

Marco Cocchi
Università Campus Bio-Medico
Maria Beatrice Falasconi
Università Campus Bio-Medico
Martina Campoli
Università Campus Bio-Medico
Lorenzo De Paola
Università Campus Bio-Medico
Leone Mazzeo
Università Campus Bio-Medico
Gioele Galieti
ENEA Casaccia Research Centre
Vincenzo Piemonte
Università Campus Bio-Medico
Stefano Vecchio Ciprioti
stefano.vecchio@uniroma1.it
Sapienza University of Rome
Riccardo Tuffi
ENEA Casaccia Research Centre

Research Article

Keywords: zeolite, ammonium ion exchange, NH4 + decomposition, Brønsted acidity, thermal analysis, silica-to-alumina ratio

Posted Date: November 18th, 2026

DOI: https://doi.org/10.21203/rs.3.rs-11524268/v1

License: This work is licensed under a Creative Commons Attribution 4.0 International License.
Read Full License

Additional Declarations: No competing interests reported.

An Innovative Thermal Decomposition Method for the Deter-mination of Exchangeable NH_4^+ in Zeolites and SAR Estimation

Marco Cocchi[1], Maria Beatrice Falasconi[1], Martina Campoli[1], Lorenzo De Paola[1], Leone Mazzeo[1], Gioele Galieti[2], Vincenzo Piemonte[1], Stefano Vecchio Ciprioti[3,*], Riccardo Tuffi[2,*]

[1] Departmental Faculty of Engineering, Chemical-Physics Fundamentals in Chemical Engineering research unit, Campus Bio-Medico University, Via Alvaro del Portillo 21, 00128, Rome, Italy; l.mazzeo@unicampus.it (L:M.), lorenzo.depaola@unicampus.it (L.D.P), m.campoli@unicampus.it (M.C.), maria.falasconi@unicampus.it (M.B.F), m.cocchi@unicampus.it (M.C.); v.piemonte@unicampus.it (V.P.).

[2] Department for Sustainability, ENEA, Casaccia Research Center, Via Anguillarese 301, 00123, S. Maria di Galeria, Rome, Italy; gioelegalieti@gmail.com

[3] Department of Basic and Applied Sciences for Engineering, Sapienza University, Via del Castro Laurenziano 7, 00161, Rome, Italy

* Correspondence: riccardo.tuffi@enea.it; Tel.: +39-06-30484335 (R.T.). stefano.vecchio@uniroma1.it; Tel.: +39-06-4976-6906 (S.V.C.).

Abstract

In this study, a thermal decomposition method (TDM) was developed for the direct determination of the concentration of exchangeable NH_4^+ ions in zeolites, based on liquid-phase NH_4^+ ion exchange followed by NH_3 desorption using a simultaneous thermogravimetry/differential scanning calorimetry (TG/DSC) instrument. The concentration of exchangeable NH_4^+ determined by TDM can be correlated with the concentration of Brønsted acid sites. Compared with conventional NH_3 temperature-programmed desorption (NH_3-TPD), the proposed method avoids the direct handling of gaseous ammonia during the adsorption step and improves reproducibility by relying on the thermal decomposition of NH_4^+ counterions introduced through ion exchange. After preliminary TG coupled with Fourier Transform Infrared Spectroscopy (TG/FTIR) experiments to identify the water and NH_3 desorption ranges, TDM was applied to commercial zeolites with SAR values ranging from 2 to 30.5. The concentration of exchangeable NH_4^+ decreased with increasing SAR, from 13,670 ± 650 μmol $NH_4^+ \cdot g^{-1}$ for 4A zeolite to 1,590 ± 90 μmol $NH_4^+ \cdot g^{-1}$ for ZSM-5. Conversely, the average decomposition energy of NH_4^+ increased with SAR, from 40 kJ·mol NH_3^{-1} for 4A to approximately 160 kJ·mol NH_3^{-1} for Y zeolite with a SAR of 12, consistently with its possible interpretation as an indicator of apparent acid strength. A semi-empirical model correlating the concentration of exchangeable NH_4^+ with SAR was also calibrated using commercial crystalline zeolites. External validation using a Y zeolite with a SAR of 12 predicted a SAR of 11.04, with a relative deviation of 8%. The method was also applied to a partially amorphous X-type zeolite synthesized from coal fly ash (X/CFA), which exhibited an exchangeable NH_4^+ concentration and average decomposition energy comparable to those of commercial 13X, equal to 11,100 μmol $NH_4^+ \cdot g^{-1}$ and 70 kJ·mol NH_3^{-1}, respectively. Overall, TDM represents a practical and reproducible method for the direct determination of the concentration of exchange-able NH_4^+ ions in zeolites, which can be correlated with the concentration of Brønsted acid sites. The method also provides information on the energy associated with the thermal decomposition of NH_4^+ and, through the proposed semi-empirical model, enables SAR estimation from the experimentally measured concentration of exchangeable NH_4^+.

Keywords: zeolite; ammonium ion exchange, NH4 + decomposition, Brønsted acidity; thermal analysis; silica-to-alumina ratio

Introduction

Zeolites are crystalline microporous solids widely used in numerous chemical processes, ranging from industrial catalytic conversions to gas adsorption [1,2]. Among their many applications, hydrocarbon cracking reactions are typically catalyzed by zeolites, whose activity arises from the presence of acid sites located both on the external surface and within the cavities. From a structural perspective, zeolites are composed of SiO_4 and AlO_4 tetrahedra connected through shared oxygen atoms [3]. Their crystalline structure can be described in terms of two levels of repeating units. The primary building units (PBUs) consist of individual silica and alumina tetrahedra, whereas secondary building units (SBUs) are three-dimensional arrangements formed by the connection of PBUs through shared oxygen atoms. One of the most common SBUs is the β-cage, also known as the sodalite cage, consisting of 24 tetrahedral PBUs arranged in four- and six-membered rings surrounding a central cavity. At the macroscopic level, SBUs are periodically organized within the three-dimensional structure, giving rise to a system of micropores. The presence of Al atoms in the framework introduces a negative charge, which is compensated by positively charged species consisting of atomic or molecular ions located within the cavities. These species, commonly referred to as extra-framework cations, are stabilized by electrostatic interactions and are responsible for the excellent ion-exchange properties of zeolites. When the charge-compensating cation is a proton, H^+, a bridging hydroxyl group is formed between silicon and aluminum, giving rise to a catalytically active Brønsted acid site [4–6].

However, different types of acid sites may coexist within the zeolite structure. Lewis acid sites, which are non-protonic in nature, are typically associated with metal cations, such as Na^+, acting as charge-compensating species [7–9]. In addition, several mechanisms have been proposed for the formation of Lewis acid sites, including the involvement of extra-framework aluminum species [10–12].

The silica-to-alumina molar ratio (SAR) plays a fundamental role in defining the composition and structure of zeolites. Variations in SAR affect the organization of the structural units and lead to the formation of different zeolite frameworks. Among the numerous structures known, those of major industrial relevance include the faujasite (FAU) framework, typically found at low to intermediate SAR values in zeolites A, X, and Y, and the MFI framework, characteristic of medium- to high-SAR zeolites such as ZSM-5 [13,14]. Since SAR reflects the aluminum content of the framework, it represents a fundamental parameter in zeolite synthesis and is directly related to the acid properties of the material. Therefore, SAR provides a first indication of the acidic character of a zeolite and represents an important descriptor for its characterization.

The acidity of zeolites has been characterized using several techniques, including infrared spectroscopy [15–17] and adsorption-based methods [18,19], which are among the most widely used approaches. Adsorption methods are based on the interaction between acid sites and suitable probe molecules. Basic molecules such as carbon monoxide (CO), acetonitrile (CH_3CN), ammonia (NH_3), trimethylamine ($N(CH_3)_3$), and pyridine (C_5H_5N) are commonly used because of their ability to interact with acid centers [20]. In particular, ammonia adsorption followed by temperature-programmed desorption (NH_3-TPD), often coupled with microcalorimetry, is commonly used to evaluate both the concentration and strength of acid sites [6,20–22]. However, this method presents several practical limitations, including the need for vacuum conditions during sample preparation and the hazardous handling of gaseous ammonia. Furthermore, when used as a standalone technique, NH_3-TPD may not provide an unambiguous quantification of the total acidity of zeolites. Indeed, NH_3 adsorption can be affected by the nature and concentration of charge-compensating cations, such as Na^+, as well as by the distribution and accessibility of acid sites. Consequently, zeolites characterized by the same SAR may exhibit different apparent acid-site concentrations when characterized by NH_3-TPD [23]. Therefore, a method capable of directly quantifying the concentration of exchangeable NH_4^+ ions and the energy associated with their thermal decomposition is of interest, as these quantities can subsequently be related to the acidic properties of the material.

In this work, we present a method for the characterization of exchangeable NH_4^+ ions in zeolites, based on liquid-phase NH_4^+ ion exchange of zeolites in the Na^+ form, when the materials are not already available in the NH_4^+ form, followed by ammonia desorption using a simultaneous TG/DSC instrument. It is important to note that this approach is not directly applicable to zeolites already available in the H^+ form since the method requires the presence of NH_4^+ or exchangeable Na^+ cations that can be replaced by NH_4^+. This approach, referred to as the Thermal Decomposition Method (TDM), provides a practical alternative for quantifying the concentration of exchangeable NH_4^+ and the energy associated with their thermal decomposition. Since NH_3 release results from the thermal decomposition of NH_4^+ ions introduced through ion exchange, the measured NH_4^+ concentration can be correlated with the concentration of Brønsted acid sites generated following thermal decomposition. In the case of crystalline zeolites, the NH_4^+ concentration can also be correlated with SAR. On this basis, a semi-empirical mathematical model was developed, calibrated, and validated using commercial crystalline zeolites. The resulting model provides a calibration curve correlating the concentration of exchangeable NH_4^+ with SAR and can therefore be used to estimate the unknown SAR of crystalline zeolites from TDM measurements.

Finally, TDM was applied to a partially amorphous X-type zeolite synthesized in the laboratory, denoted as X/CFA, obtained from coal fly ash (CFA), an abundant and low-cost source of SiO_2 and Al_2O_3 for zeolite synthesis [24]. The catalytic performance of X/CFA in the pyrolysis of real polyolefin plastic waste has already been demonstrated [25,26], making this material a suitable case study for exploring the potential of TDM for the quantification of exchangeable NH_4^+ ions in zeolitic materials characterized by a significant amorphous fraction.

Materials and Methods

This section describes the methodological approach used to develop the Thermal Decomposition Method (TDM) for zeolites in the NH_4^+ form. The commercial and laboratory-synthesized zeolites analyzed are initially presented, together with the ion-exchange procedure used to convert the selected samples from the Na^+ form to the NH_4^+ form. The characterization procedure is then described, from the preliminary identification of the NH_3 desorption temperature range to the determination of the concentration of exchangeable NH_4^+ and the energy associated with its thermal decomposition by TG/DSC analysis. Finally, the semi-empirical mathematical model is introduced, including its derivation, parameter estimation, and validation procedure.

Materials

The commercial zeolites used in this work were selected to cover a wide range of silica-to-alumina molar ratios (SAR). The selected set ranged from Na-form zeolite 4A, with a SAR of 2, to NH_4-form ZSM-5, with a SAR of 30.5. Four different zeolite structures were considered: zeolite A, characterized by β-cages; zeolites X and Y, both belonging to the FAU framework; and ZSM-5, representative of the MFI framework. Among these materials, zeolites with SAR values of 2, 2.6, 5.1 and 30.5 were used for model parameter estimation, whereas the zeolite with a SAR of 12 was used for model validation. The complete list of commercial zeolites included in the dataset, together with their known properties and supplier information, is reported in Table 1. As indicated by the suppliers, product specifications are subject to revision and may vary over time.

Table 1

The laboratory-synthesized zeolite used in this study was produced from coal fly ash (CFA) collected at a coal gasification plant in Kolkata (India), following the synthesis procedure described by Verrecchia et al. [27]. The resulting material was a NaX zeolite, hereafter referred to as

NaX/CFA. Some properties of the synthesized zeolite are re-ported in Table 2. Since the application of the method requires the NH_4^+ form of the zeolites, as described in Section 2.2.2, the commercial 4A and 13X zeolites, together with X/CFA, were subjected to ion exchange with NH_4Cl (Clean Consult International, Lodi, Italy), following the procedure reported by Cocchi et al. [25]. In this work, NH_4^+ ex-change was assumed to be quantitative according to the adopted exchange protocol.

Table 2

Characterization procedure based on thermal decomposition of NH_4^+ ions

The concentration of exchangeable NH_4^+ ions and the energy associated with their thermal decomposition were investigated by performing TG/DSC measurements on the selected zeolites in their NH_4^+ form. The method is based on the thermal desorption of NH_3 from NH_4^+-form zeolites according to a specific heating program, resulting in the formation of the corresponding H^+-form zeolites. The mass loss and the energy involved during NH_3 release are related to the concentration of NH_4^+ ions present in the sample and to the energy associated with their thermal decomposition, respectively, as discussed in Section 2.3. The procedure consists of two main steps, described in the following sections and schematically illustrated in Figure 1.

Figure 1

First Phase: TG and FTIR analysis of ammonium thermal decomposition.

NH_3 desorption experiments were performed using a simultaneous thermogravimetric analysis/differential scanning calorimetry (TG/DSC) instrument (Mettler-Toledo, TG/DSC1) coupled via a transfer line to a gas-phase FTIR spectrometer (Thermo Fisher Scientific, Nicolet iS10). This first stage of the procedure (Figure 1) consisted of preliminary experiments aimed at identifying the temperature range over which NH_3 desorption occurs selectively. The separation of NH_3 desorption from the release of other species, mainly water, is essential for the accurate quantification of NH_4^+ ions based on the NH_3 released during their decomposition. For this purpose, the evolved gases were analyzed by FTIR spectroscopy. Spectra were acquired every 11 s using eight scans over a spectral range of 0.5 cm^{-1} and at a resolution of 4 cm^{-1}, allowing the NH_3 desorption profile to be monitored and distinguished from water desorption.

Approximately 70 mg of NH_4^+-form zeolite were placed in a 150 µL alumina crucible inside the simultaneous TG/DSC instrument. Nitrogen was used as the carrier gas at a flow rate of 60 $mL \cdot min^{-1}$. The temperature program consisted of a single heating ramp from 30 °C to 500 °C at a

rate of 5 °C·min^{-1}. Blank experiments were performed under the same experimental conditions using an empty alumina crucible, in order to correct the baseline by accounting for gas buoyancy effects.

Second Phase: quantitative determination of NH_4^+ exchange concentration and thermal decomposition energy.

The second step, corresponding to the actual NH_3 desorption method, was aimed at quantifying the concentration of exchangeable NH_4^+ and the energy associated with its thermal decomposition using a TG/DSC analyzer (Figure 1). Once the temperature range associated with NH_3 desorption had been distinguished from that corresponding to water release, NH_3 desorption was quantified by simultaneously measuring the energy required by the process.

The experiments were performed using a Mettler-Toledo TG/DSC1 instrument. Nitrogen was used as the purge gas at a flow rate of 30 mL·min^{-1}. Approximately 5 mg of NH_4^+-form zeolite was placed in a 100 µL aluminum crucible. The temperature program consisted of an initial heating ramp from 30 °C to 130 °C at 5 °C·min^{-1}, followed by an isothermal step of 50 min at 130 °C. Subsequently, a second heating ramp from 130 °C to 500 °C was applied at 10 °C·min^{-1}, followed by a final isothermal step of 35 min at 500 °C. These temperature values are consistent with the main literature reports concerning the thermal desorption of ammonia from zeolites [28,29].

Two different blank experiments were performed for the TG and DSC analyses, respectively. The TG blank was carried out under the same experimental conditions using an empty aluminum crucible. In contrast, the DSC blank was performed by repeating the experiment using the same crucible containing the zeolite sample remaining after NH_3 desorption, i.e., the zeolite in its H^+ form. In this DSC blank experiment, the zeolite was not removed from the crucible in order to account for the heat required to increase the temperature of the sample, i.e., the sensible heat. This contribution was subsequently subtracted from the raw DSC signal to isolate the heat associated exclusively with the thermal decomposition of NH_4^+ and the consequent release of NH_3.

Experimental determination of exchangeable NH_4^+ concentration and thermal decomposition energy

Using the TDM, two parameters were determined: the concentration of exchangeable NH_4^+ and the energy associated with its thermal decomposition.

Since NH_3 desorption results from the thermal decomposition of NH_4^+ counter-ions into NH_3 and H^+, the concentration of NH_4^+ can be determined from the amount of NH_3 released during the

thermal treatment. Assuming that each NH_4^+ ion results in the re-lease of one NH_3 molecule, the concentration of exchangeable NH_4^+ was determined from the mass loss attributable to NH_3 occurring during the thermal decomposition of the NH_4^+-form zeolite, according to Eq. 1.

$$\mathrm{NH_4^+\ exchangeable}\ [\mu\mathrm{mol}\cdot \mathrm{g}_{\mathrm{zeolite}}^{-1}] = \frac{\left(\frac{m(t_a)-m(t_b)}{MW_{\mathrm{NH_3}}}\cdot 10^6\right)}{m(t_{\mathrm{fin}})} \qquad (1)$$

In Eq. 1, m(t) represents the residual sample mass [mg] as a function of time t [s], where t = 0 corresponds to the beginning of the experiment. The parameters t_a and t_b represent the times at which NH_3 desorption starts and ends, respectively, whereas t_{fin} denotes the final time of the experiment; therefore, $m(t_{fin})$ corresponds to the mass of the zeolite in its H^+ form. Finally, MW_{NH_3} denotes the molecular weight of NH_3, equal to 17 g·mol^{-1}.

While the mass loss measured by TG was used to quantify the amount of NH_3 released, the simultaneous DSC signal was used to evaluate the energy associated with the thermal decomposition of NH_4^+. This quantity was used as an energetic parameter of the process and subsequently as a potential indicator of apparent acid strength.

The DSC signal represents the instantaneous heat flow, $tp(t)$, as a function of time [mJ·s^{-1}], with negative values corresponding to heat absorbed by the material. As described in a previous section, the DSC blank experiments were performed using the spent zeolite in its H^+ form, which remained in the same crucible after NH_3 desorption. The corrected heat flow, $ntp(t)$, was therefore obtained by subtracting the blank signal, $btp(t)$, from the raw DSC signal of the NH_4^+-form zeolite.

The cumulative energy associated with the thermal decomposition of NH_4^+, $E(t)$, was then calculated by integrating the corrected DSC signal over the NH_3 desorption interval, between t_a and t_b:

$$E(t)\ [mJ] = \int_{t_a}^{t_b} ntp(\tau)d\tau \qquad (2)$$

At each time t within the NH_3 desorption interval, the corresponding amount of desorbed ammonia was calculated from the TG mass loss according to Eq. 3:

$$n_{NH_3}(t) = \frac{m(t)-m(t_a)}{MW_{NH_3}} \qquad (3)$$

where $m(t_a)$ is the sample mass at the beginning of NH_3 desorption, $m(t)$ is the sample mass at time t, and MW_{NH_3} is the molar mass of ammonia.

By associating each value of $E(t)$ with the corresponding value of $n_{NH_3}(t)$, the thermal decomposition energy can be directly expressed as a function of the amount of NH_3 desorbed, $E(n_{NH_3}(t))$. The specific decomposition energy of NH_4^+ was therefore defined as the energy associated with the release of one mole of NH_3. Since this quantity depends on the coverage of the sites by NH_3, it was calculated as the derivative of the decomposition energy with respect to the amount of NH_3 desorbed:

$$Specific\ Decomposition\ Energi\ of\ NH_4^+\ (n_{NH3})[kJ \cdot mol_{NH3}^{-1}] = -\frac{d\ E(n_{NH3})}{d\ n_{NH3}} \quad (4)$$

where E is expressed in kJ.

To compare the zeolites using a single representative parameter, the average decomposition energy of NH_4^+ was calculated by averaging the specific decomposition energy over the entire NH_4^+ decomposition range, from zero to the maximum amount, $n_{MAX\ NH3}$:

$$Average\ decomposition\ energy\ of\ NH_4^+\ [kJ \cdot mol_{NH3}^{-1}] = \frac{\int_0^{n_{MAX\ NH3}} Specific\ Decomposition\ Energi\ of\ NH_4^+\ (n_{NH3})[kJ \cdot mol_{NH3}^{-1}]}{n_{MAX\ NH3}} \quad (5)$$

Semi-empirical modelling of exchangeable NH_4^+ concentration as a function of SAR

A theoretical expression for the concentration of exchangeable NH_4^+ species was initially derived from the composition of the zeolite framework, considering the relationship between the number of framework Al atoms and the number of negative charges compensated by NH_4^+ ions. The model is based on the assumption that the zeolite framework can be ideally described as a repetition of AlO_2 and SiO_2 units homogeneously distributed throughout the structure. In this simplified framework, each AlO_2 unit is associated with one negative charge and, assuming quantitative ion exchange, with one compensating NH_4^+ ion, while the local Si/Al ratio is assumed to be equal to the average value of the bulk zeolite.

Since the silica-to-alumina molar ratio is defined as SAR = SiO_2/Al_2O_3, the corresponding Si/Al atomic ratio is equal to SAR/2. Accordingly, the theoretical amount of exchangeable NH_4^+ can be expressed as (Eq. 6):

$$\text{theoretical } NH_4^+ \text{ exchange concentration } [\mu mol \cdot g_{zeolite}^{-1}] = \frac{10^6}{\left(MW_{uAl} + \frac{SAR}{2} \cdot MW_{uSi}\right)} \quad (6)$$

Where MW_{uAl} represents the molecular weight of the AlO_2 unit associated with one negative charge, whereas MW_{uSi} represents the molecular weight of the SiO_2 unit. The values of MW_{uAl} and MW_{uSi} are 58.98 and 60.09 g·mol^{-1}, respectively. The resulting expression is therefore based on the assumption that the amount of exchangeable NH_4^+ can be correlated with the SAR, independently of the specific framework topology. The model represents an idealized stoichiometric description of the zeolite framework and does not explicitly account for framework topology, aluminium distribution, framework defects or extra-framework species. Consequently, deviations from the theoretical prediction may be expected in real zeolites.

Since the theoretical expression does not fully account for the actual structural complexity of zeolites, the molar masses MW_{uAl} and MW_{uSi} were treated as adjustable parameters. This approach allows the model to account for deviations arising from framework defects, extra-framework species, and differences between the nominal and actual zeolite compositions. Accordingly, the functional dependence between the SAR and the amount of exchangeable NH_4^+ was reformulated in the following semi-empirical form (Eq. 7):

$$\text{NH}_4^+ \text{ exchange concentration } [\mu mol \cdot g_{zeolite}^{-1}] = \frac{10^6}{(a + SAR/2 \cdot \text{b})} \quad (7)$$

where a and b are the fitting parameters estimated from the experimental values of exchangeable NH_4^+. The theoretical model was initially applied without fitting parameters to assess its predictive capability against the experimentally measured exchangeable NH_4^+ values. The semi-empirical model was subsequently calibrated by nonlinear regression using the least-squares method. The regression was performed on the experimental exchangeable NH_4^+ values obtained for the commercial zeolites, with the exception of sample Y2. This zeolite was selected because its SAR value of 12 is intermediate relative to those of all the samples analyzed in this study. It was therefore excluded from parameter estimation and instead used as an external validation sample to assess the predictive performance of the calibrated model.

Results and Discussion

TG and FTIR analysis of ammonium thermal decomposition

In the first step of the procedure (Figure 1), NH_4-13X zeolite was used as reference material to identify the temperature ranges associated with water and ammonia desorption. The results are reported in Figure 2, which shows the TG curve and its time derivative (DTG) for NH_4-13X. Two main DTG peaks can be observed at 103 °C and 179 °C. These peaks were assigned to the desorption of water and ammonia, respectively. Their partial overlap indicates that water and ammonia desorption are not completely separated during the initial heating stage. Above approximately 350 °C, the desorption rate progressively decreases, and the process can be considered complete at 500 °C, where the DTG signal approaches zero.

Figure 2

The identification of the evolved species was carried out by FTIR analysis of the gases released during the TG experiment. The FTIR spectrum collected at 103 °C, corresponding to the first DTG peak, is reported in Figure 3. The spectrum clearly shows the presence of water, as confirmed by comparison with its characteristic absorption bands reported in the same figure. Water release at this temperature is expected, since zeolites can readily adsorb moisture from the atmosphere

Figure 3

At 130 °C, the DTG curve exhibits an intermediate minimum in the desorption rate between the two main peaks (Figure 2). The corresponding FTIR spectra highlighted a decrease in the water signal, together with the first evidence of ammonia absorption bands, indicating the onset of NH_3 desorption (FTIR spectrum not shown). Ammonia release becomes clearly evident at the second DTG peak, centered at 179 °C.

The FTIR spectrum of the evolved gases collected at this temperature is reported in Figure 3 and confirms the presence of NH_3, identified by its characteristic absorption bands at 965 and 930 cm^{-1} [31]. Moreover, comparison with the characteristic water absorption regions, namely 1100–2000 cm^{-1} and 3500-4000 cm^{-1} [32], indicates that water is no longer detected at this temperature. These results show that 130 °C represents a suitable transition temperature between the dehydration stage and the beginning of NH_3 desorption. Therefore, in the subsequent TDM experiments, the mass loss occurring after the dehydration step and up to 500 °C can be mainly ascribed to NH_3 released from the NH_4^+-form zeolite. This preliminary investigation thus provides the basis for separating the contribution of water from that of ammonia and for accurately quantifying the concentration of exchangeable NH_4^+ determined by TG/DSC analysis.

329

330 *Exchangeable NH_4^+ concentration of commercial zeolites determined by TDM*

331

332 The second step, corresponding to the actual NH_3 desorption method, was defined on the basis of
333 the results obtained in the preliminary TG/FTIR investigation. As described in a previous section,
334 the heating program was designed to separate NH_3 desorption from water release by introducing an
335 intermediate isothermal step at 130 °C. After preliminary tests, an isothermal time of 50 min was
336 considered suitable to ensure effective water removal. As an example of the TG/DTG results
337 obtained during this step, the curves recorded for the NH_4-13X zeolite are reported in Figure 4.

338

339 Figure 4

340

341 The TG curve shows a progressive decrease in mass with increasing temperature. In particular,
342 water desorption can be considered almost complete during the isothermal step at 130 °C.
343 Consequently, the mass loss occurring during the subsequent heating ramp can be mainly attributed
344 to NH_3 desorption. The final isothermal step at 500 °C results in a second plateau in the mass curve,
345 indicating that NH_3 desorption is complete. A similar behavior was observed for the other
346 commercial zeolites investigated in this study.
347 According to Eq. 1, the mass change measured during this second stage of the TG experiment was
348 used to calculate the concentration of exchangeable NH_4^+ in the zeolites. The values obtained for
349 the entire set of commercial zeolites are reported in Table 3. As expected, both the NH_3 mass loss
350 and the corresponding concentration of exchangeable NH_4^+ decrease with increasing SAR. The
351 highest NH_3 mass loss was observed for zeolite 4A, characterized by the lowest SAR value (SAR =
352 2), with a mass loss of 23.2 wt% and an exchangeable NH_4^+ concentration of 13,670 μmol
353 $NH_4^+ \cdot g^{-1}$. In contrast, ZSM-5, with the highest SAR value (SAR = 30.5), exhibited the lowest NH_3
354 mass loss, equal to 2.7 wt%, corresponding to an exchangeable NH_4^+ concentration of 1,590 μmol
355 $NH_4^+ \cdot g^{-1}$.
356 This trend is consistent with the expected relationship between the aluminium content of the zeolite
357 framework and the amount of charge-compensating NH_4^+ counterions. As the SAR increases, the
358 number of Al atoms incorporated into the zeolite framework decreases, resulting in a lower
359 concentration of charge-compensating NH_4^+ ions and, consequently, in a reduced release of NH_3
360 during thermal decomposition [19,33–35].

361

Table 3

The parameters of the semi-empirical model were estimated by a least-squares regression method using the experimental values of the exchangeable NH_4^+ concentration obtained for the commercial zeolites, excluding sample Y2, which was reserved for external model validation. As reported in Table 4, the regression yielded values of 10.88 ± 4.77 $g \cdot mol^{-1}$ and 62.92 ± 1.36 $g \cdot mol^{-1}$ for parameters a and b, respectively, with a regression coefficient (R^2) of 0.998. This result indicates that the semi-empirical model accurately describes the experimental relationship between SAR and exchangeable NH_4^+ concentration over the investigated compositional range.

Table 4

For comparison, the exchangeable NH_4^+ concentration values obtained in this work are reported in Figure 5 together with literature data from Engtrakul et al. [36] and Hunger et al. [23,28], where acidity was determined from the amount of NH_3 desorbed by NH_3-TPD, along with the theoretical prediction curve described by Eq. 6. The Y2 sample is also included in the figure to provide a graphical representation of the validation point.

Figure 5

The theoretical model satisfactorily describes the exchangeable NH_4^+ concentration of both the zeolites investigated in this study and the NH_4^+-form literature samples that meet the assumptions of Eq. 6. In these materials, each framework Al atom associated with an exchangeable counterion can be associated, assuming quantitative exchange, with one charge-compensating NH_4^+ ion. The theoretical curve therefore represents the maximum theoretical concentration of exchangeable NH_4^+ expected from the framework composition.

Samples characterized by incomplete NH_4^+/Na^+ exchange fall below this curve, since the released ammonia accounts only for the fraction exchanged with NH_4^+ and is therefore not representative of the total amount of sites occupied by charge-compensating counterions. The agreement between the model and the experimental data is particularly good for SAR > 20, whereas increasing deviations are ob-served at lower SAR values, with experimental values exceeding the theoretical prediction.

This deviation may reflect the limitations of the simplified model as the Al content increases. In addition, at low SAR values, a contribution of experimental origin cannot be ruled out: the higher hydrophilicity of these zeolites may promote the retention of re-sidual water, whose mass loss could

be partially attributed to NH_3 desorption. Similarly, the possible presence of residual NH_4Cl originating from the ion-exchange procedure and not completely removed during washing could contribute to the measured amount of NH_3. These contributions may therefore contribute to the observed overestimation relative to the theoretical prediction, particularly for low-SAR samples. For this reason, the semi-empirical model was introduced to describe the experimental trend using fitted parameters, without imposing an exclusively theoretical description of the system.

In addition to the comparison with the theoretical prediction, Figure 5 also highlights an important methodological aspect. Literature data [34] obtained by NH_3-TPD show that different acidity values may be reported at similar SAR values. TDM offers a specific advantage in this regard, as the liquid-phase ion-exchange step allows the ex-changeable Na^+ ions to be replaced with NH_4^+ prior to thermal decomposition, making the released NH_3 directly related to the exchangeable NH_4^+ concentration.

For zeolites in the NH_4^+ form, TDM and NH_3-TPD are expected to provide comparable values, since both methods ideally probe the same population of sites. The small deviations observed, with TDM yielding slightly higher values, may be related to the NH_3 adsorption step preceding TPD analysis. Despite the good reproducibility of the measurements, NH_3 adsorption is not necessarily complete and may be affected by operating conditions such as the adsorption temperature and NH_3 partial pressure [37]. Therefore, NH_3-TPD may slightly underestimate the concentration of acid sites, whereas TDM directly quantifies exchangeable NH_4^+ ions through the NH_3 released during thermal treatment. This makes the experimental procedure simpler and potentially more reliable, enabling, in the case of crystalline zeolites, the construction of a calibration curve relating the exchangeable NH_4^+ concentration to SAR. The agreement between the fitted curve and the Y2 validation point further supports the reliability of the model. For Y2, the model predicts a SAR value of 11.04, corresponding to a relative deviation of 8% from the expected value of 12. This result confirms that the proposed model can provide a reliable estimate of the SAR of crystalline zeolites from TDM measurements of the exchangeable NH_4^+ concentration.

Energy characterization of NH_4^+ decomposition in Commercial Zeolites

The second part of the acidity characterization focused on the evaluation of the energy associated with the thermal decomposition of NH_4^+ species, subsequently used as a possible indicator of the apparent acid strength of the zeolite samples. As an example, Figure 6 reports the DSC results obtained for zeolite 13X, including the raw heat-flow signal of the sample in the NH_4^+ form, *tp(t)*,

429 the blank signal measured on the corresponding exhausted sample in the H^+ form, *btp(t)*, and the
430 resulting net heat-flow signal, *ntp(t)*.
431 The raw and blank DSC curves exhibit an overall similar trend, mainly associated with the heat
432 required to increase the temperature of the sample. However, the thermal contribution associated
433 with NH_3 desorption is present only in the raw DSC signal recorded for the zeolite in the NH_4^+
434 form. Therefore, to isolate the contribution of NH_3 desorption from the sensible heat of the sample,
435 the net heat-flow signal was calculated as the difference between *tp(t)* and *btp(t)*. The resulting
436 *ntp(t)* curve, also shown in Figure 6, was then used to calculate the energy associated with the
437 thermal decomposition of NH_4^+ species and the subsequent desorption of NH_3**.** The same procedure
438 was applied to all the zeolite samples investigated.
439
440 Figure 6
441
442 The net heat-flow signal exhibited a similar profile for all the zeolite samples investigated. In
443 general, an initial endothermic peak was observed during the early heating stage, followed by a
444 second, more intense endothermic peak during the subsequent heating ramp. The first contribution
445 can be mainly attributed to the desorption of residual water, whereas the second peak is associated
446 with the heat absorbed during NH_3 desorption from the zeolite. The net heat-flow signal was
447 therefore integrated over the NH_3 desorption interval and combined with the corresponding amount
448 of desorbed NH_3, as described in Section 2.3. Using Eq. 4, the specific decomposition energy of
449 NH_4^+ decomposition was calculated as a function of the amount of NH_3 released. As an example,
450 the specific decomposition energy $of\ NH_4^+$ curve obtained for zeolite 13X is shown in Figure 7 as
451 a function of the moles of desorbed NH_3.
452 As discussed previously, higher values of the specific decomposition energy indicate that a greater
453 amount of energy is required for NH_3 release. This parameter can therefore be considered as a
454 possible indicator of the apparent acid strength. Acid strength is commonly evaluated using basic
455 probe molecules, and ammonia is widely employed as a descriptor of acidity. Furthermore, acid
456 strength has been correlated with the activation energy of reactions catalyzed by zeolites [38–41].
457 However, this apparent acid strength does not represent a single intrinsic property of the zeolite
458 sample, but rather depends on the NH_3 coverage, i.e., the fraction of acid sites occupied by NH_3
459 molecules [42–44].
460
461 Figure 7
462

As shown in Figure 7 for zeolite 13X, the specific decomposition energy increases as the NH_3 coverage decreases. This behavior indicates that, as desorption proceeds, the remaining NH_3 molecules are progressively associated with stronger interactions and therefore require a greater amount of energy to be desorbed. To compare the investigated zeolites, the specific decomposition energy profile was summarized using the average decomposition energy. For zeolite 13X, the decomposition energy remains close to its average value over almost 80% of the total amount of desorbed NH_3, corresponding to approximately 8000 μmol $NH_3 \cdot g^{-1}$, as shown in Figure 7. This behavior is consistent with the acid-strength profiles reported in the literature [33].

Accordingly, the zeolite set was compared by calculating the average decomposition energy over the entire NH_3 coverage range, according to Eq. 5. The values obtained from the experimental DSC data are reported in Table 5.

Table 5

The average decomposition energy values showed a clear correlation with the SAR: higher SAR values corresponded to higher average decomposition energies. This trend is consistent with previous studies reporting that high-silica protonic zeolites generally exhibit greater Brønsted acid strength than alumina-rich protonic zeolites [45–47], sup-porting the possible interpretation of decomposition energy as an indicator of apparent acid strength.

The lowest average decomposition energy was measured for zeolite 4A, with a value of 40 kJ· mol NH_3^{-1}. As the SAR increased, the average decomposition energy progressively increased, reaching approximately 164 kJ·mol NH_3^{-1} for zeolite Y2. Zeolite Y1 exhibited an intermediate value of 112 kJ· mol NH_3^{-1}. Comparable values, around 110 kJ· mol NH_3^{-1}, were reported by Chong Liu et al. [48] for low-silica faujasite zeolites using ammonia as a probe molecule.

The observed increase may be related to changes in the local electronic environment of framework Al atoms. In particular, as the density of Al atoms within the siliceous framework decreases, variations in their electronegativity and in the surrounding Si–O–Al environment may lead to stronger Brønsted acid sites, as also discussed by Chong Liu et al. [48].

For the high-SAR ZSM-5 zeolite, the determination of NH_4^+ decomposition energy, and consequently its interpretation in terms of apparent acid strength, was not considered reliable. In this case, the low amount of desorbed NH_3 resulted in large deviations in the values derived from DSC measurements, preventing a robust quantitative assessment.

TDM characterization of the laboratory-synthesized X/CFA zeolite

Following calibration of the semi-empirical model using four commercial zeolites, namely 4A, 13X, Y1, and ZSM-5, and its validation using the commercial Y2 zeolite, the laboratory-synthesized X/CFA zeolite was characterized by TDM**.** The concentration of exchangeable NH_4^+ species and the decomposition energy associated with their thermal decomposition determined for this material are reported in Table 6.

Table 6

X/CFA exhibits a concentration of exchangeable NH_4^+ ions and an average decomposition energy comparable to those of the commercial zeolite 13X. In particular, the concentration of exchangeable NH_4^+ in X/CFA is 11,100 μmol $NH_4^+ \cdot g^{-1}$, which is very close to the value measured for 13X, namely 10,600 μmol $NH_4^+ \cdot g^{-1}$. A similar agreement was also observed in terms of average decomposition energy, with values of 70 kJ·mol NH_3^{-1} for X/CFA and 73 kJ·mol NH_3^{-1} for 13X. This comparison is particularly relevant because both materials belong to the FAU framework family. However, previous characterization of X/CFA by XRD analysis, surface area measurements, and CO_2 adsorption indicated a synthesis yield of approximately 60 wt% [27]. This suggests that a significant fraction of the material may remain non-crystalline or only partially converted. There-fore, the similarity between X/CFA and commercial 13X in terms of exchangeable NH_4^+ concentration cannot be readily explained by considering only the crystalline zeolitic fraction and warrants further discussion.

One possible explanation is that the amorphous or poorly crystalline aluminosilicate fraction of X/CFA may also contribute, at least partially, to the measured amount of exchangeable NH_4^+. Previous studies have shown that the development of Brønsted acidity does not necessarily require a fully crystalline zeolitic framework, although the concentration and strength of Brønsted acid sites in amorphous aluminosilicates are generally lower than those in crystalline zeolites [49,50]. Furthermore, Aguayo et al. [42] reported that the presence of an amorphous phase does not necessarily prevent access to acid sites associated with the crystalline zeolitic fraction. On this basis, the high NH_4^+ concentration measured for X/CFA may arise from two concurrent contributions: ex-changeable sites associated with the crystalline FAU phase and a possible contribution from exchangeable sites present in the amorphous aluminosilicate fraction.

It is important to emphasize that this interpretation remains preliminary. The available data do not allow the individual contributions of the crystalline and amorphous phases to be quantitatively separated. Nevertheless, the results suggest that the TDM approach based on ion exchange may detect exchangeable sites present in both fractions, thereby providing an overall measure of

exchangeable NH_4^+ concentration that is not exclusively limited to crystalline zeolitic domains. This aspect is particularly noteworthy and should be further investigated in future studies by combining TDM with complementary techniques capable of distinguishing between sites associated with the crystalline and amorphous phases.

For X/CFA, the application of the semi-empirical model for SAR estimation should be treated with caution, as the model was developed and validated exclusively for crystalline zeolites. The partially amorphous nature of the material prevents the overall ex-changeable NH_4^+ concentration from being directly interpreted using the calibrated relationship between NH_4^+ concentration and SAR established for crystalline zeolites. Nevertheless, extending the model to X/CFA yielded an apparent SAR of 2.51, in agreement with the composition of the CFA precursor and with values characteristic of X-type zeolites.

Overall, the results obtained for X/CFA demonstrate that TDM can also be applied to a partially amorphous aluminosilicate material to determine the overall concentration of exchangeable NH_4^+ and the energy associated with its thermal decomposition. The values obtained are comparable to those of the commercial zeolite 13X. The NH_4^+ con-centration can be related to the concentration of Brønsted acid sites generated following thermal decomposition, whereas the decomposition energy may be regarded as a potential indicator of apparent acid strength. These findings are also consistent with the promising catalytic performance previously reported for X/CFA in the cracking and pyrolysis of polyolefinic plastic waste [25,26,52].

Conclusions

In this investigation, a thermal decomposition method (TDM) was developed for the determination of exchangeable NH_4^+ concentration and NH_4^+ decomposition energy in zeolites, based on ion exchange with NH_4^+ in the liquid phase followed by NH_3 desorption using a simultaneous TG/DSC instrument. The TDM was applied to commercial zeolites characterized by a wide range of SAR values, from 2 to 30.5. As expected, the concentration of exchangeable NH_4^+ decreased with increasing SAR. The highest value was measured for zeolite 4A, amounting to 13,670 ± 650 μmol $NH_4^+ \cdot g^{-1}$, whereas ZSM-5 with a SAR of 30.5 exhibited the lowest NH_4^+ concentration, equal to 1,590 ± 90 μmol $NH_4^+ \cdot g^{-1}$. Intermediate values were obtained for zeolites 13X, Y1, and Y2, amounting to 10,600 ± 300, 5,800 ± 60, and 2,790 ± 40 μmol $NH_4^+ \cdot g^{-1}$, respectively. The concentration of ex-changeable NH_4^+ can be related to the concentration of Brønsted acid sites generated upon thermal decomposition.

The DSC signal was used to evaluate the energy associated with the thermal de-composition of NH_4^+, which was considered as a potential indicator of apparent acid strength. The average decomposition energy increased with increasing SAR, consistently with the higher Brønsted acidity generally reported for silica-rich zeolites. The lowest value was obtained for zeolite 4A, amounting to 40 kJ·mol NH_3^{-1}, whereas zeolite Y2, with a SAR of 12, reached approximately 160 kJ·mol NH_3^{-1}. Zeolite 13X exhibited an average decomposition energy of 73 kJ·mol NH_3^{-1}.

A semi-empirical model correlating the concentration of exchangeable NH_4^+ with SAR was developed and calibrated using crystalline commercial zeolites. The regression yielded fitting parameters of $a = 10.88 \pm 4.77$ g·mol^{-1} and $b = 62.92 \pm 1.36$ g·mol^{-1}, with $R^2 = 0.998$, confirming that the model accurately describes the experimental relationship between exchangeable NH_4^+ concentration and SAR. Zeolite Y2 was excluded from the calibration procedure and used as an external validation sample. For this zeolite, the model predicted a SAR of 11.04, corresponding to a relative deviation of 8% from the expected value of 12. These results demonstrate that the main objective of the study was achieved: the TDM-based calibration model can be used to estimate the SAR of un-known crystalline zeolites from the experimentally measured concentration of ex-changeable NH_4^+.

The method was also applied to X/CFA zeolite synthesized in the laboratory from coal fly ash. Despite its partially amorphous nature, X/CFA yielded TDM results com-parable to those obtained for commercial 13X, with an exchangeable NH_4^+ concentration of 11,100 µmol $NH_4^+ \cdot g^{-1}$ and an average decomposition energy of 70 kJ·mol NH_3^{-1}. An apparent SAR value of 2.51 was obtained by applying the model outside its original calibration domain. This value is close to that of the CFA precursor and consistent with the range typically reported for X-type zeolites. This result suggests that TDM may also provide useful information for zeolitic materials containing a significant amorphous fraction, although this aspect requires further investigation.

Future work should focus on expanding the calibration dataset by including additional crystalline zeolites with different framework structures and intermediate SAR values, in order to improve the robustness of the calibration curve. In parallel, the ap-plication of TDM to partially amorphous zeolitic materials should be further investigated to clarify the contribution of crystalline and amorphous aluminosilicate phases to the measured exchangeable acidity.

References

1. Corma, A. State of the art and future challenges of zeolites as catalysts, *J. Catal.* **2003**, *216,* 298–312. https://doi.org/10.1016/S0021-9517(02)00132-X.
2. Busca, G. Acid Catalysts in Industrial Hydrocarbon Chemistry, *Chem. Rev*. **2007**, *107*, 5366–5410. https://doi.org/10.1021/cr068042e.
3. Maxwell, I.E.; Stork, W.H.J. Chapter 17 Hydrocarbon processing with zeolites, in: 2001: pp. 747–819. https://doi.org/10.1016/S0167-2991(01)80259-7.
4. Haag, W.O.; Lago, R.M.; Weisz, P.B. The active site of acidic aluminosilicate catalysts, *Nature*. **1984**, *309*, 589–591. https://doi.org/10.1038/309589a0.
5. Jones, A.J.; Carr, R.T.; Zones, S.I.; Iglesia, E. Acid strength and solvation in catalysis by MFI zeolites and effects of the identity, concentration and location of framework heteroatoms, *J. Catal.* **2014**, *312*, 58–68. https://doi.org/10.1016/j.jcat.2014.01.007.
6. Lee, C.; Parrillo, D.J.; Gorte, R.J.; Farneth, W.E. Relationship between Differential Heats of Adsorption and Brønsted Acid Strengths of Acidic Zeolites: H-ZSM-5 and H-Mordenite, *J. Am. Chem. Soc.* **1996**, *118*, 3262–3268. https://doi.org/10.1021/ja953452y.
7. Silva, B.; Figueiredo, H.; Soares, O.S.G.P.; Pereira, M.F.R.; Figueiredo, J.L.; Lewandowska, A.E.; Bañares, M.A.; Neves, 0 I.C.; Tavares, T. Evaluation of ion exchange-modified Y and ZSM5 zeolites in Cr(VI) biosorption and catalytic oxidation of ethyl acetate, *Appl. Catal. B Environ*. **2012**, *117–118*, 406–413. https://doi.org/10.1016/j.apcatb.2012.02.002.
8. Liao, J.; Zhang, Y.; Fan, L.; Chang, L.; Bao, W. Insight into the Acid Sites over Modified NaY Zeolite and Their Adsorption Mechanisms for Thiophene and Benzene, *Ind. Eng. Chem. Res*. 2019, 58, 4572–4580. https://doi.org/10.1021/acs.iecr.8b05046.
9. Li, S.; Zheng, A.; Su, Y.; Zhang, H.; Chen, L.; Yang, J.; Ye, C.; Deng, F. Brønsted/Lewis Acid Synergy in Dealuminated HY Zeolite: A Combined Solid-State NMR and Theoretical Calculation Study, *J. Am. Chem. Soc.* **2007**, *129*, 11161–11171. https://doi.org/10.1021/ja072767y.
10. Brus, J.; Kobera, L.; Schoefberger, W.; Urbanová, M.; Klein, P.; Sazama, P.; Tabor, E.; Sklenak, S.; Fishchuk, A. V.; Dědeček, J. Structure of Framework Aluminum Lewis Sites and Perturbed Aluminum Atoms in Zeolites as Determined by 27 Al{ 1 H} REDOR (3Q) MAS NMR Spectroscopy and DFT/Molecular Mechanics, Angew. Chemie Int. Ed. (2014) n/a-n/a. https://doi.org/10.1002/anie.201409635.
11. Zhang, Y.; Zhao, R.; Sanchez-Sanchez, M.; Haller, G.L.; Hu, J.; Bermejo-Deval, R.; Liu, Y.; Lercher, J.A. Promotion of protolytic pentane conversion on H-MFI zeolite by proximity of extra-framework aluminum oxide and Brønsted acid sites, *J. Catal*. **2019**, *370*, 424–433.

https://doi.org/10.1016/j.jcat.2019.01.006.
12. Ravi, M.; Sushkevich, V.L.; van Bokhoven, J.A. Lewis Acidity Inherent to the Framework of Zeolite Mordenite, *J. Phys. Chem. C.* **2019**, *123*, 15139–15144. https://doi.org/10.1021/acs.jpcc.9b03620.
13. Barthomeuf, D. Basic Zeolites: Characterization and Uses in Adsorption and Catalysis, *Catal. Rev*. **1996**, *38*, 521–612. https://doi.org/10.1080/01614949608006465.
14. Morales-Pacheco, P.; Domínguez, J.M.; Bucio, L.; Alvarez, F.; Sedran, U.; Falco, M. Synthesis of FAU(Y)- and MFI(ZSM5)-nanosized crystallites for catalytic cracking of 1,3,5-triisopropylbenzene, *Catal. Today*. **2011**, *166*, 25–38. https://doi.org/10.1016/j.cattod.2010.07.005.
15. Gabrienko, A.A.; Danilova, I.G.; Arzumanov, S.S.; Pirutko, L.V.; Freude, D.; Stepanov, A.G. Direct Measurement of Zeolite Brønsted Acidity by FTIR Spectroscopy: Solid-State 1 H MAS NMR Approach for Reliable Determination of the Integrated Molar Absorption Coefficients, *J. Phys. Chem. C*. **2018**, *122*, 25386–25395. https://doi.org/10.1021/acs.jpcc.8b07429.
16. Kotrel, S.; Lunsford, J.H.; Knözinger, H. Characterizing Zeolite Acidity by Spectroscopic and Catalytic Means: A Comparison, *J. Phys. Chem. B*. **2001**, *105*, 3917–3921. https://doi.org/10.1021/jp002161v.
17. Zholobenko, V.; Freitas, C.; Jendrlin, M;. Bazin, P.; Travert, A.; Thibault-Starzyk, F. Probing the acid sites of zeolites with pyridine: Quantitative AGIR measurements of the molar absorption coefficients, *J. Catal.* **2020**, *385*, 52–60. https://doi.org/10.1016/j.jcat.2020.03.003.
18. Katada, N.; Suzuki, K.; Noda, T.; Park, M.B.; Min, H.-K.; Hong, S.B.; Niwa, M. Ammonia IRMS-TPD Characterization of Brønsted Acid Sites in Medium-pore Zeolites with Different Framework Topologies, *Top. Catal*. **2010**, *53*, 664–671. https://doi.org/10.1007/s11244-010-9503-y.
19. Lónyi, F.; Valyon, J. On the interpretation of the NH3-TPD patterns of H-ZSM-5 and H-mordenite, *Microporous Mesoporous Mater*. **2001**, *47*, 293–301. https://doi.org/10.1016/S1387-1811(01)00389-4.
20. Kustov, L.M. New trends in IR-spectroscopic characterization of acid and basic sites in zeolites and oxide catalysts, *Top. Catal*. **1997**, *4*, 131–144. https://doi.org/10.1023/A:1019136121724.
21. Brunner, E.; Beck, K.; Koch, M.; Heeribout, L.; Karge, H.G. Verification and quantitative determination of a new type of Brønsted acid sites in H-ZSM-5 by 1H magic-angle spinning nuclear magnetic resonance spectroscopy, *Microporous Mater*. **1995**, 3, 395–399.

https://doi.org/10.1016/0927-6513(94)00052-W.
22. Karge, H.G. Concepts and Analysis of Surface Acidity and Basicity, in: Handb. Heterog. Catal., Wiley-VCH Verlag GmbH & Co. KGaA, Weinheim, Germany, 2008. https://doi.org/10.1002/9783527610044.hetcat0057.
23. Hunger, B.; Heuchel, M.; Clark, L.A.; Snurr, R.Q. Characterization of acidic OH groups in zeolites of different types: An interpretation of NH3-TPD results in the light of confinement effects, *J. Phys. Chem. B*. **2002**, *106*, 3882–3889. https://doi.org/10.1021/jp012688n.
24. Wdowin, M.; Franus, M.; Panek, R.; Badura, L.; Franus, W. The conversion technology of fly ash into zeolites, *Clean Technol. Environ. Policy*. **2014**, *16*, 1217–1223. https://doi.org/10.1007/s10098-014-0719-6.
25. Cocchi, M.; De Angelis, D.; Mazzeo, L.; Nardozi, P.; Piemonte, V.; Tuffi, R.; Vecchio Ciprioti, S. Catalytic pyrolysis of a residual plastic waste using zeolites produced by coal fly ash, Catalysts. 10 (2020) 1–17. https://doi.org/10.3390/catal10101113.
26. Cocchi, M.; Cafiero, L.; De Angelis, D.; Falasconi, M.B.; Vecchio Ciprioti, S. Conversion of marine plastic litter into chemicals and fuels through catalytic pyrolysis using commercial and coal fly ash synthesized zeolites, Under Rev. - ACS Sustain. Chem. Eng. (2022).
27. Verrecchia, G.; Cafiero, L.; de Caprariis, B.; Dell'Era, A.; Pettiti, I.; Tuffi, R;. Scarsella, M. Study of the parameters of zeolites synthesis from coal fly ash in order to optimize their CO_2 adsorption, *Fuel*. **2020**, *276*, 118041. https://doi.org/10.1016/j.fuel.2020.118041.
28. Hunger, B.; Hoffmann, J.; Heitzsch, O.; Hunger, M. Temperature-programmed desorption (TPD) of ammonia from HZSM-5 zeolites, *J. Therm. Anal.* **1990**, *36*, 1379–1391. https://doi.org/10.1007/BF01914061.
29. Hoffmann, J.; Dombrowski, D. Temperature programmed desorption of NH_3 and H_2O from NH_4NaX and $CoNH_4NaX$ zeolites, *React. Kinet. Catal. Lett.* **1982**, *21*, 485–490. https://doi.org/10.1007/BF02095846.
30. Busca, G. Acidity and basicity of zeolites: A fundamental approach, *Microporous Mesoporous Mater*. **2017**, *254*, 3–16. https://doi.org/10.1016/j.micromeso.2017.04.007.
31. France, W.L.; Williams, D. Total Absorptance of Ammonia in the Infrared, *J. Opt. Soc. Am*. **1966**, *56*, 70–74. https://doi.org/10.1364/JOSA.56.000070.
32. Hakkarainen, T;. Mikkola, E.; Laperre, J.; Gensous, F.; Fardell, P.; Tallec, Y.; Baiocchi, C.; Paul, K.; McNamee, M.; Deleu, C.; Metcalfe, E. Smoke gas analysis by Fourier Transform Infrared Spectroscopy – Summary of the SAFIR project results, *Fire Mater*. **2000**, *24*, 101–112. https://doi.org/10.1002/1099-1018(200003/04)24:23.3.CO;2-U.
33. Deka, R. Ch., Acidity in zeolites and their characterization by different spectroscopic

methods, *Indian J. Chem. Technol*. **1998**, *5*, 109–123.
34. Marakatti, V.S.; Gaigneaux, E.M. Alkylation of resorcinol with tertiary butanol over zeolite catalysts: Shape selectivity vs acidity, *Catal. Commun*. **2021**, *152*, 106291. https://doi.org/10.1016/j.catcom.2021.106291.
35. C. Hidalgo, Measurement of the acidity of various zeolites by temperature-programmed desorption of ammonia, *J. Catal.* **1984**, *85*, 362–369. https://doi.org/10.1016/0021-9517(84)90225-2.
36. Engtrakul, C.; Mukarakate, C.; Starace, A.K.; Magrini, K.A.; Rogers, A.K.; Yung, M.M. Effect of ZSM-5 acidity on aromatic product selectivity during upgrading of pine pyrolysis vapors, *Catal. Today.* **2016**, *269*, 175–181. https://doi.org/10.1016/j.cattod.2015.10.032.
37. Helminen, J.; Helenius, J.; Paatero, E.; Turunen, I. Comparison of sorbents and isotherm models for NH3-gas separation by adsorption, *AIChE J.* **2000**, *46*, 1541–1555. https://doi.org/10.1002/aic.690460807.
38. Brogaard, R.Y.; Wang, C.-M.; Studt, F. Methanol–Alkene Reactions in Zeotype Acid Catalysts: Insights from a Descriptor-Based Approach and Microkinetic Modeling, *ACS Catal.* **2014**, *4*, 4504–4509. https://doi.org/10.1021/cs5014267.
39. Wang, C.-M.; Brogaard, R.Y.; Weckhuysen, B.M.; Nørskov, J.K.; Studt, F. Reactivity Descriptor in Solid Acid Catalysis: Predicting Turnover Frequencies for Propene Methylation in Zeotypes, *J. Phys. Chem. Lett*. **2014**, *5*, 1516–1521. https://doi.org/10.1021/jz500482z.
40. Borges, P.; Ramos Pinto, R.; Lemos, M.A.N.D.A.; Lemos, F.; Védrine, J.C.; Derouane, E.G.; Ramôa Ribeiro, F. Activity–acidity relationship for alkane cracking over zeolites: n-hexane cracking over HZSM-5, *J. Mol. Catal. A Chem*. **2005**, *229*, 127–135. https://doi.org/10.1016/j.molcata.2004.11.012.
41. Katada, N.; Sota, S.; Morishita, N.; Okumura, K.; Niwa, M. Relationship between activation energy and pre-exponential factor normalized by the number of Brønsted acid sites in cracking of short chain alkanes on zeolites, *Catal. Sci. Technol*. **2015**, *5*, 1864–1869. https://doi.org/10.1039/C4CY01483A.
42. Aguayo, A.T.; Gayubo, A.G.; Vivanco, R.; Olazar, M.; Bilbao, J. Role of acidity and microporous structure in alternative catalysts for the transformation of methanol into olefins, *Appl. Catal. A Gen*. **2005**, *283*, 197–207. https://doi.org/10.1016/j.apcata.2005.01.006.
43. Arandes, J.M.; Abajo, I.; López-Valerio, D.; Fernández, I.; Azkoiti, M.J;. Olazar, M.; Bilbao, J. Transformation of Several Plastic Wastes into Fuels by Catalytic Cracking, *Ind. Eng. Chem. Res.* **1997**, *36*, 4523–4529. https://doi.org/10.1021/ie970096e.
44. Elordi, G.; Olazar, M.; Artetxe, M.; Castaño, P.; Bilbao, J. Effect of the acidity of the HZSM-

5 zeolite catalyst on the cracking of high density polyethylene in a conical spouted bed reactor, *Appl. Catal. A Gen*. **2012**, *415–416*, 89–95. https://doi.org/10.1016/j.apcata.2011.12.011.

45. Barthomeuf, D. Zeolite acidity dependence on structure and chemical environment. Correlations with catalysis, Mater. Chem. Phys. 17 (1987) 49–71. https://doi.org/10.1016/0254-0584(87)90048-4.

46. Katada, N.; Kageyama, Y.; Takahara, K.; Kanai, T.; Ara Begum, H.; Niwa, M. Acidic property of modified ultra stable Y zeolite: increase in catalytic activity for alkane cracking by treatment with ethylenediaminetetraacetic acid salt, *J. Mol. Catal. A Chem*. **2004**, *211*, 119–130. https://doi.org/10.1016/j.molcata.2003.10.001.

47. Parrillo, D.J.; Gorte, R.J. Characterization of acidity in H-ZSM-5, H-ZSM-12, H-Mordenite, and H-Y using microcalorimetry, *J. Phys. Chem*. **1993**, *97*, 8786–8792. https://doi.org/10.1021/j100136a023.

48. Liu, C.; Tranca, I.; van Santen, R.A.; Hensen, E.J.M.; Pidko, E.A. Scaling Relations for Acidity and Reactivity of Zeolites, *J. Phys. Chem. C*. **2017**, *121*, 23520–23530. https://doi.org/10.1021/acs.jpcc.7b08176.

49. Hensen, E.J.M.; Poduval, D.G.; Ligthart, D.A.J.M.; Van Veen, J.A.R.; Rigutto, M.S. Quantification of strong brønsted acid sites in aluminosilicates, *J. Phys. Chem. C*. **2010**, *114*, 8363–8374. https://doi.org/10.1021/jp9106348.

50. Poduval, D.G.; Van Veen, J.A.R.; Rigutto, M.S.; Hensen, E.J.M. Brønsted acid sites of zeolitic strength in amorphous silica-alumina, *Chem. Commun*. **2010**, *46*, 3466–3468. https://doi.org/10.1039/c000019a.

51. Tanaka, H.; Sakai, Y.; Hino, R. Formation of Na-A and -X zeolites from waste solutions in conversion of coal fly ash to zeolites, *Mater. Res. Bull*. **2002**, *37*, 1873–1884. https://doi.org/10.1016/S0025-5408(02)00861-9.

52. Occasi, G.; De Angelis, D.; Scarsella, M.; Tammaro, M.; Tuccinardi, L.; Tuffi, R. Recovery material from a new designed surgical face mask: A complementary approach based on mechanical and thermo-chemical recycling, *J. Environ. Manage*. **2022**, *324*, 116341. https://doi.org/10.1016/j.jenvman.2022.116341.

Abbreviations

The following abbreviations are used in this manuscript:

MDPI	Multidisciplinary Digital Publishing Institute
DOAJ	Directory of open access journals
TLA	Three-letter acronym
LD	Linear dichroism

764

765

766 **Table 1**.

767 Commercial zeolites characteristics (supplier data) in the form of powders.

Zeolite	SAR (mol/mol)	Pore size (Å)	Cation type	BET surface area (m^2/g)	Supplier Company
4A	2	4	Na^+	560 [b]	Sigma-Aldrich
13X	2.6 [a]	10	Na^+	865 [c]	Alfa Aesar
Y1	5.1	7	NH_4^+	n.a.	Alfa Aesar
Y2	12	7	NH_4^+	730 [b]	Alfa Aesar
ZSM-5	30.5	5÷6	NH_4^+	400 [b]	Alfa Aesar

768 [a] Supplier did not provide this information. SAR was taken from literature (Jang et al. 2025;
769 Kim and Kim 2023).
770 [b] Data from supplier
771 [c] Verrecchia et al. 2020 [27]
772 n.a. = not available
773

774 **Table 2**. X/CFA characteristics (Verrecchia et al. [27] in the form of a powder.

Zeolite	Origin CFA	NaX Yield (%)	Cation type	BET surface area (m^2/g)
X/CFA	Kolkata (India)	60	Na^+	498

775
776

777

778 **Table 3**. TG zeolite characterization results

Zeolite	SiO_2/Al_2O_3 [mol/mol]	$\Delta mass_{NH_3}$ [wt%]	Exchangeable NH_4^+ concentration [$\mu mol_{NH_3} \cdot g^{-1}$]

LTA *Structure*	4A	2	23.2 ± 1.1	13,670 ± 650
FAU *Structure*	13X	2.6	18.1 ± 0.5	10,600 ± 300
	Y1	5.1	9.7 ± 0.1	5,800 ± 60
	Y2	12	4.6 ± 0.1	2,790 ± 40
MFI *Structure*	ZSM-5	30.5	2.7 ± 0.2	1,590 ± 90

Table 4. Regression results of the semi-empirical model for exchangeable NH_4^+ concentration.

Regression method	a [g mol^{-1}]	b [g mol^{-1}]	R^2
Least square	10.88 ± 4.77	62.92 ± 1.36	0.998

Table 5. Average decomposition energy values of NH_4^+ for the zeolite samples

Zeolite		SiO_2/Al_2O_3 [mol/mol]	Average decomposition energy of NH_4^+ [kJ·mol$_{NH_3}^{-1}$]
LTA *Structure*	4A	2	40
FAU *Structure*	13X	2.6	73
	Y1	5.1	112
	Y2	12	164

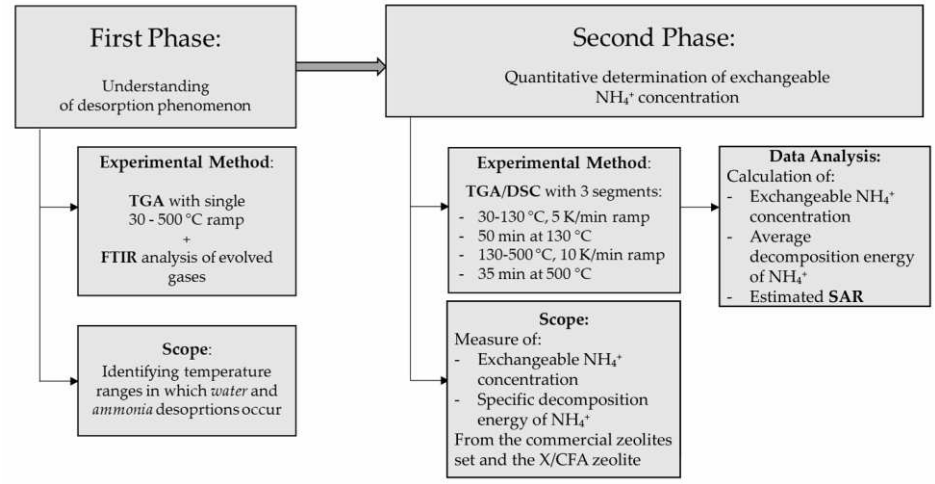
Caption to the figures

Figure 1. Scheme reporting the acid investigation procedure is divided into two main phases.

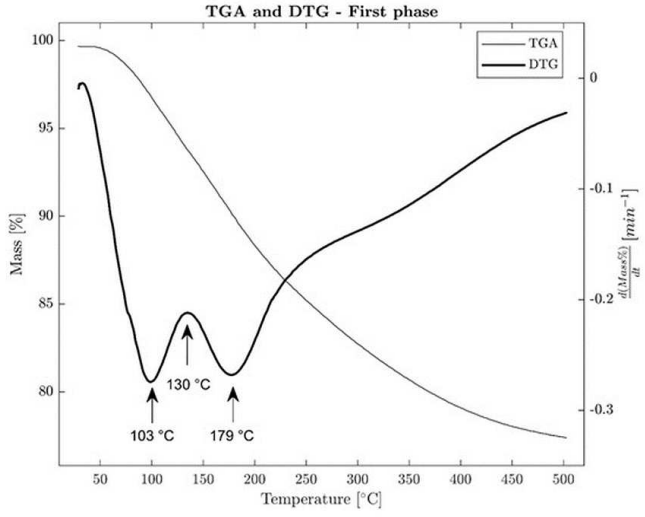
Figure 2. TG and DTG curves of NH_4-13X Zeolite in a single 30–500 °C ramp at 5 °C·min^{-1}. The DTG curves show 2 peaks that corresponds to water (103 °C) and ammonia (179 °C) desorption respectively.

Figure 3. FTIR analysis of evolved gases from NH_4-13X zeolite during a single heating ramp from 30 to 500 °C at 5 °C min^{-1}. (a) Gram-Schmidt curve with the temperatures selected for gas-phase characterization; (b) FTIR spectrum at 103 °C showing water evolution (measured spectrum compared with the OMNIC reference spectrum); (c) FTIR spectrum at 179 °C showing ammonia evolution (measured spectrum compared with the OMNIC reference spectrum).

798 **Figure 4.** TG/DTG curves vs. time of 13X zeolite sample resulting from the application of the
799 heating program developed for the characterization of the second phase. Temperature program is
800 also reported.
801 **Figure 5.** Comparison between the exchangeable NH_4^+ concentration measured in this work by
802 TDM and literature NH3-TPD data (reported as NH_4^+-equivalent amounts) as a function of SAR.
803 The theoretical prediction curve and the semi-empirical model developed in this study are also
804 reported. The Y2 sample, excluded from the regression procedure, is shown as an external
805 validation point of the semi-empirical model.
806 **Figure 6.** Representation of raw sample thermal power, *tp*(*t*), blank experiment thermal power,
807 btp(t), and net sample thermal power ntp(t) for 13-X zeolite.
808
809
810
811



812 **Figure 1.** Scheme reporting the acid investigation procedure is divided into two main phases.



813
814 **Figure 2**. TG and DTG curves of NH_4-13X Zeolite in a single 30–500 °C ramp at 5 °C·min^{-1}. The
815 DTG curves show 2 peaks that corresponds to water (103 °C) and ammonia (179 °C) desorption
816 respectively.

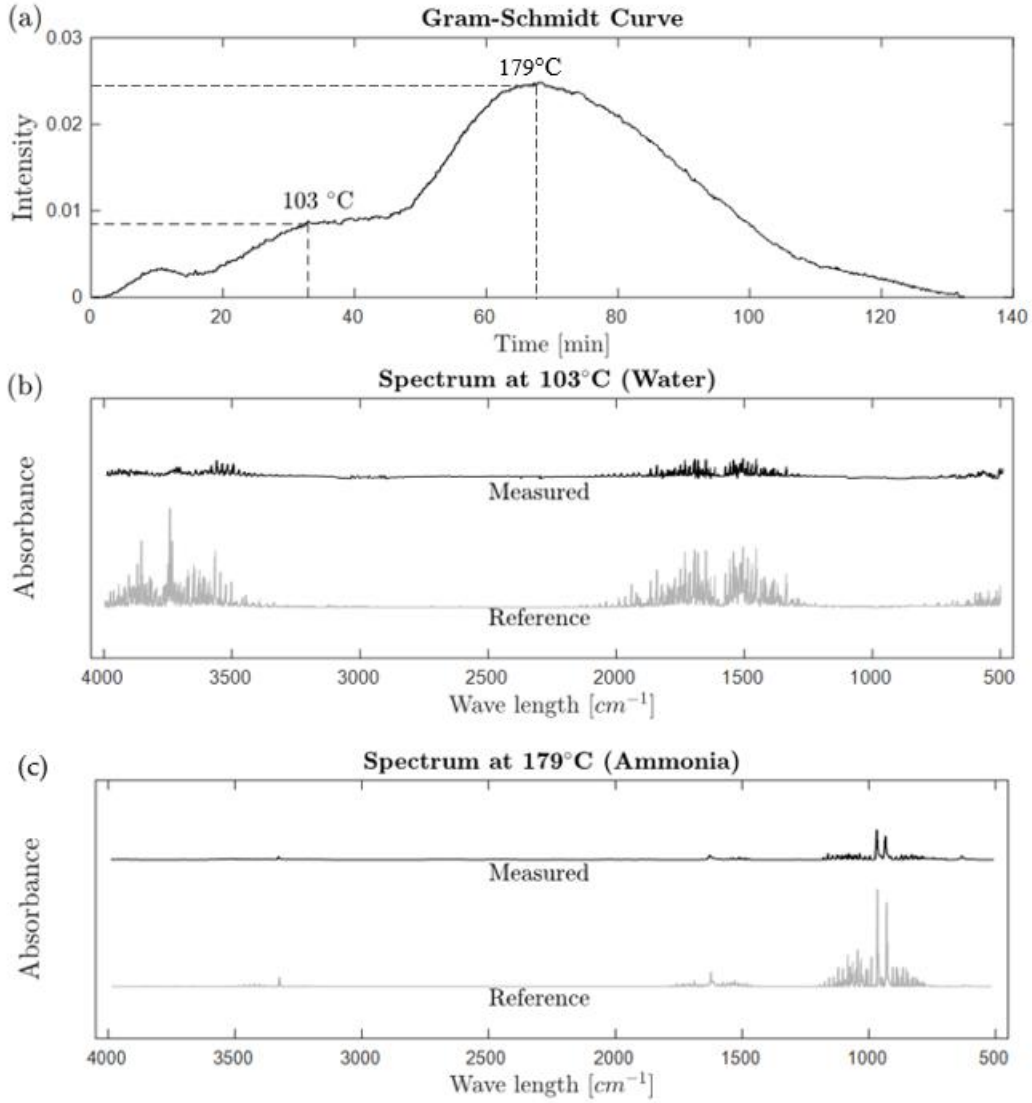
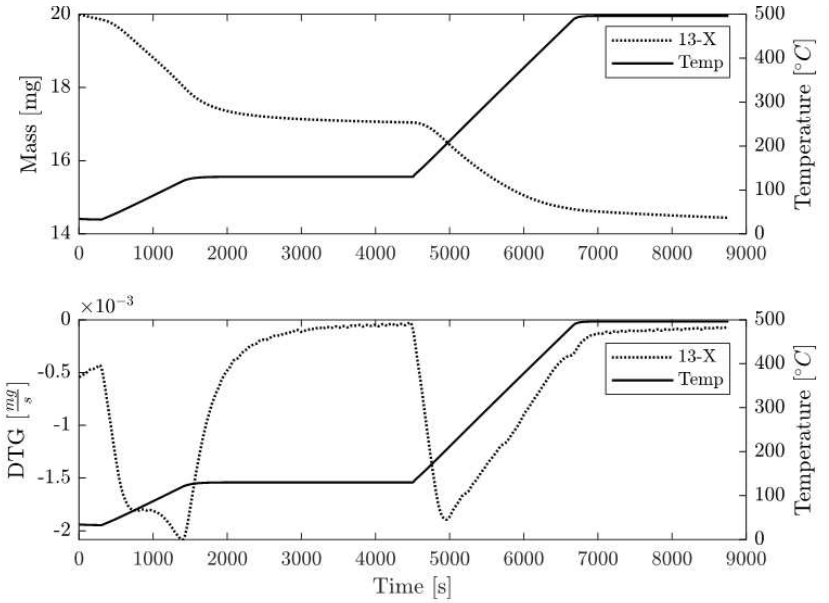
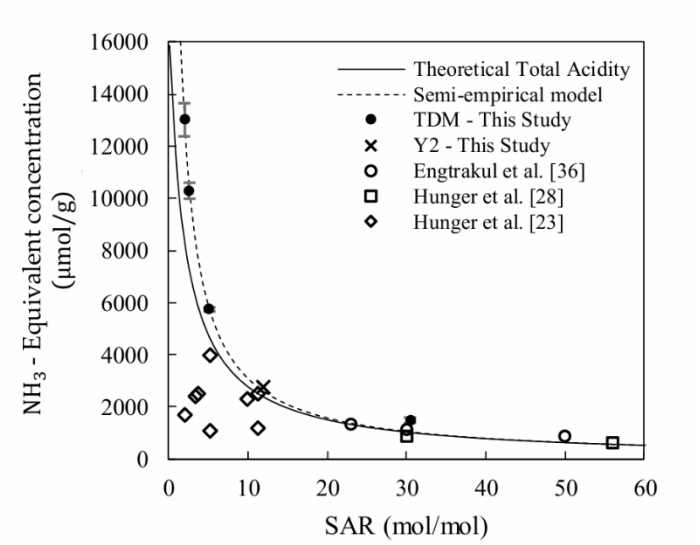


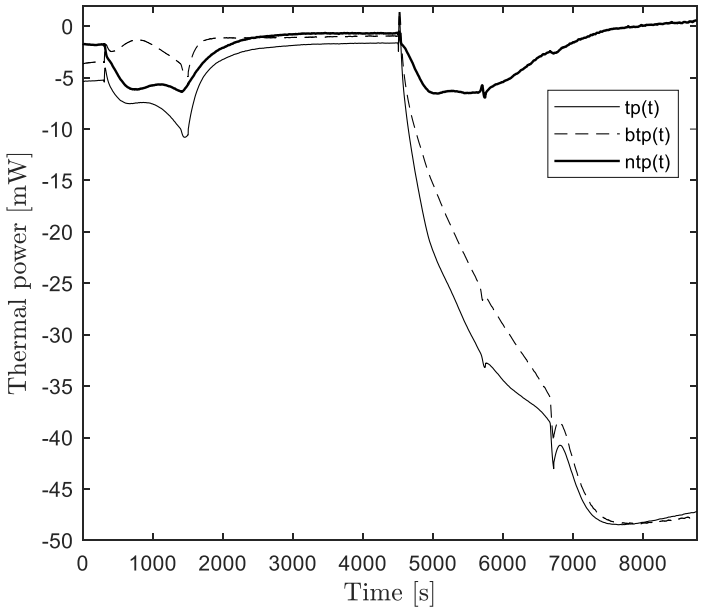
Figure 3. FTIR analysis of evolved gases from NH_4-13X zeolite during a single heating ramp from 30 to 500 °C at 5 °C min^{-1}. (a) Gram-Schmidt curve with the temperatures selected for gas-phase characterization; (b) FTIR spectrum at 103 °C showing water evolution (measured spectrum compared with the OMNIC reference spectrum); (c) FTIR spectrum at 179 °C showing ammonia evolution (measured spectrum compared with the OMNIC reference spectrum).



827 **Figure 4.** TG/DTG curves vs. time of 13X zeolite sample resulting from the application of the
828 heating program developed for the characterization of the second phase. Temperature program is
829 also reported.
830



831
832 **Figure 5.** Comparison between the exchangeable NH_4^+ concentration measured in this work by
833 TDM and literature NH3-TPD data (reported as NH_4^+-equivalent amounts) as a function of SAR.
834 The theoretical prediction curve and the semi-empirical model developed in this study are also
835 reported. The Y2 sample, excluded from the regression procedure, is shown as an external
836 validation point of the semi-empirical model
837



838

839 **Figure 6.** Representation of raw sample thermal power, *tp*(*t*), blank experiment thermal power,
840 btp(t), and net sample thermal power *ntp*(*t*) for 13-X zeolite.

841